Journal of Alloys and Compounds 513 (2012) 165–171

Contents lists available at SciVerse ScienceDirect

Journal of Alloys and Compounds

journal homepage: www.elsevier.com/locate/jallcom

Impedance spectroscopic characterization of fine-grained magnetoelectric $Pb(Zr_{0.53}Ti_{0.47})O_3$–$(Ni_{0.5}Zn_{0.5})Fe_2O_4$ ceramic composites

Hongfang Zhang[a,b], Chee-Leung Mak[b,*]

[a] Department of Physics, Suzhou University of Science and Technology, Suzhou 215009, China
[b] Department of Applied Physics, The Hong Kong Polytechnic University, Hung Hom, Kowloon, Hong Kong

ARTICLE INFO

Article history:
Received 16 August 2011
Received in revised form 3 October 2011
Accepted 3 October 2011
Available online 18 October 2011

Keywords:
Magnetoelectric
Composites
Conductivity
Impedance
Grain boundaries

ABSTRACT

Temperature dependent impedance spectroscopic analysis of fine-grained magnetoelectric $Pb(Zr_{0.53}Ti_{0.47})O_3$–$(Ni_{0.5}Zn_{0.5})Fe_2O_4$ (PZT–NZFO) composites was investigated. Debye-like impedance relaxation peaks were observed at intermediate frequency range. Maxwell–Wagner (MW) relaxation model was used to explain the space charge effect due to heterogeneous PZT and NZFO grain boundary in finer structure. The total resistivity was dominated by the grain boundary resistance due to the blocking effect arisen from the glass phase additive. The small value of conductivity measured in this system suggested the glass additive markedly modified the grain boundary properties. Electric modulus spectra reflected the contributions from two different effects: the large resolved semicircle arc was caused by the grain effect and the small poorly resolved semicircle arc was attributed to the grain boundary. The activation energy calculated from the impedance spectra was consistent with value estimated from the modulus spectra. Investigation on dielectric spectra revealed a polydispersive dielectric relaxation existing in the system, which was also demonstrated in the ac conductivity spectra. Small polaron relaxation and MW-type polarization mechanism were discussed through the analysis on the ac conductivity spectra.

1. Introduction

Magnetoelectric (ME) effect is defined as the phenomenon of generating a dielectric polarization inside a material under an applied magnetic field or generating an induced magnetization under an applied external electric field [1]. Due to their attractive physical properties and potential applications in actuators, transducers, magnetic field sensors and data storage devices, there has been continued interests in studying ME materials in the past decades [2–6]. Although a number of single-phase materials with intrinsic ME effect have been reported, the ME effects observed in these materials are very weak [5,6]. In contrast, a much larger extrinsic ME effect has been realized in two-phase composites caused by the interaction of magnetic and electric subsystems via elastic deformations [7]. As a result, a suitable combination of two different material phases such as magnetostrictive and piezoelectric phases yields a practically useful extrinsic ME effect in composites with ten to hundred times higher compared to the intrinsic ME effect in the single-phase multiferroic compounds. The reported composites mainly include: laminated composites of ferrite and $Pb(Zr,Ti)O_3$, $Tb_{0.3}Dy_{0.7}Fe_{1.92}$ and $Pb(Mg_{1/3}Nb_{2/3})O_3$–$PbTiO_3$, etc. [8,9] and bulk composites of nickel ferrite and $Pb(Zr,Ti)O_3$, cobalt ferrite and $BaTiO_3$, as well as $Sr_{1-9}Ca_{0-1}NaNb_5O_{15}$, etc. [10–14]. Bulk composites have the advantage of superior mechanical properties over layered composites [15]. In addition, sintered composites have been widely studied because of their simplicity in synthesis using conventional ceramic processing. In this process, one could easily control the physical, magnetic, electrical and ME properties by varying proper choices of the two phases as well as their volume fraction.

Recently, we have reported the exhibition of ME effect in fine-grained $Pb(Zr_{0.53}Ti_{0.47})O_3$–$Ni_{0.5}Zn_{0.5}Fe_2O_4$ (PZT–NZFO) bulk composites with 3–0 connectivity prepared by a modified hybrid process, in which the glass-coated nano-scaled PZT powders were acted as fillers inside the NZFO matrix [12]. Complex impedance spectroscopy is a powerful and versatile technique to analyze the microstructure–property relationship, and it also allows distinguishing between intrinsic (bulk) and extrinsic contribution (grain boundary, surface layer, and electrode contact problem). An equivalent circuit based on impedance and modulus spectra provides the physical process occurring inside the sample. Impedance spectroscopic studies of electrochemical properties of electrode alloys, [16,17], ferro-electromagnetic ceramic $Pb(Fe_{1/2}Nb_{1/2})O_3$ [18], and magnetoelectric single-phase $Bi_6Fe_2Ti_3O_{12}$ compounds [19], as well as $Pb(Zr,Ti)O_3$(PZT)/$CoFe_2O_4$(CFO) multilayers composite thin films [20,21] have been carried out; they described the connection

* Corresponding author. Tel.: +852 2766 5669; fax: +852 2333 7629.
E-mail address: apaclmak@polyu.edu.hk (C.-L. Mak).

0925-8388/$ – see front matter © 2011 Elsevier B.V. All rights reserved.
doi:10.1016/j.jallcom.2011.10.013

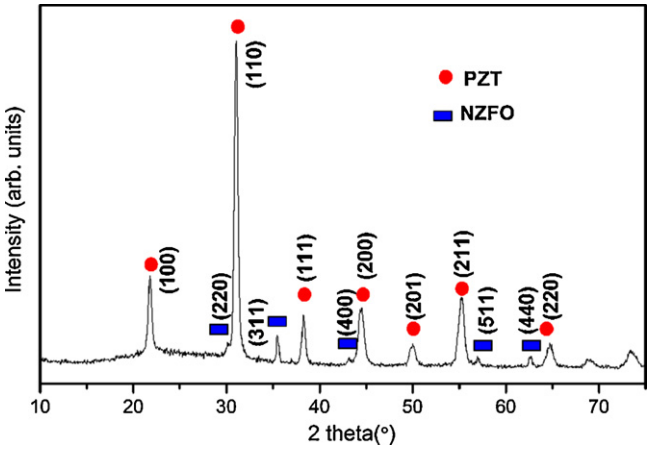

Fig. 1. X-ray diffraction pattern of the PZT–NZFO composite ceramic.

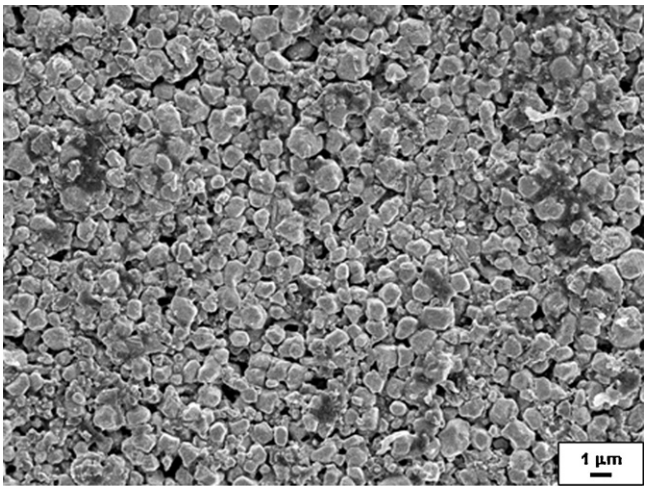

Fig. 2. Surface morphology of the PZT–NZFO composite ceramic sintered at temperature of 900 °C.

between microstructure and electrical properties and dielectric behaviors with the help of impedance spectroscopy.

In general, sintered ME composite ceramics tend to exhibit superior room temperature ferroelectric and leakage characteristics compared to the layered composite. The presence of grain boundaries in the polycrystalline sintered composites, and the defect structure (especially for finer microstructure such as interface and pores) could be one of the major factors in degradation of ferroelectric and leakage characteristics. While much attention has been paid toward enhancing the leakage characteristics and polarization, impedance spectroscopic analysis on this material has been lacking. Therefore, in order to develop a deeper understanding of the fine-scaled structure magnetoelectric PZT–NZFO ceramic composites, the impedance, modulus, dielectric and ac conductivity of such system as a function of temperature (25–200 °C) and frequency (10–10^6 Hz) were investigated. To the best of our knowledge, there are no existing reports on the effects of fine structure on the electrical properties of ME composites with small amount of amorphous glass phase as additive. In the present work, fine-grained PZT–NZFO ceramic composites were prepared by a modified hybrid process at a relatively low sintering temperature of 900 °C. The phase structures and microstructures of the bulk composites were characterized by X-ray diffraction and scanning electron microscope, respectively. Temperature and frequency dependent impedance spectroscopy were carried out in order to reveal the relaxation and polarization mechanisms in these composites.

2. Experimental

A modified hybrid process was used to prepare the fine-grained PZT–NZFO magnetoelectric ceramic composites. The details of the process have been reported elsewhere [12]. Specimen with 15 wt% of ferrite phase was sintered at 900 °C for 4 h. The phase structure and morphology of the composites were observed by X-ray diffraction (XRD, Philips X'Pert-Pro MPD) with Cu$K_{\alpha 1}$ radiation (1.5406 Å, 40 kV, 30 mA), and field emission scanning electron microscope (SEM, JEOL JSM-6335F), respectively. For electrical measurements, low temperature fired-on silver paste was applied on both sides of the ceramic composites, and then the samples were heat-treated at 600 °C for 30 min to form smooth silver electrodes. Impedance spectroscopy from 10 Hz to 1 MHz was measured at temperatures ranging from 25 to 200 °C using a Novocontrol Alpha analyzer with an ac oscillation level of 1 V. The measured temperature was kept constant with an accuracy of ±1 °C.

3. Results and discussion

3.1. Fine-scaled structure ceramic composites

Fig. 1 shows the XRD pattern of the PZT–NZFO composite. Two sets of well-defined peaks, corresponding to the magnetic (NZFO) and piezoelectric (PZT) phases, were clearly identified. As expected, the diffraction peaks arisen from the PZT phase had a stronger intensity due to the larger weight percent in the composite. The surface morphology of the composite is shown in Fig. 2. A dense, homogeneous and fully developed fine-scaled structure was observed. The grain size varied from few micrometers to several hundred of nanometers. The energy dispersive X-ray analysis indicated that grains with an average size of 1–2 μm were PZT phase and those with an average size below 500 nm were NZFO phase. The key characteristic of the hybrid process is to graft the sol–gel wet chemistry process to the conventional mixed oxide ceramic process. The high performance of ceramics prepared by conventional ceramic process under high temperatures can be mostly preserved, while the sintering temperature of the composite can be effectively reduced down as inherited from the sol–gel process. Additionally, the PZT gel solution coated by the glass phase is acted as the binding agent to connect the NZFO particles and fill the interstitials of the NZFO particles, reducing the particle-to-particle interaction for better composite performance [12].

3.2. Impedance analysis

Fig. 3(a) and (b) shows the variation of the real and imaginary parts of impedance (Z' and Z'', respectively) as a function of frequency at different temperatures varying from 100 to 200 °C. Inset in Fig. 3(b) shows the magnification of Z'' at high frequency range. As shown in Fig. 3(a), it is observed that the magnitude of Z' decreases with an increase in frequency or temperature. The Z' values for all temperatures merge to about 50 kΩ for frequencies above 100 kHz. This may be due to the release of space charges. While frequency dependence of Z' indicates dielectric relaxation process, its temperature dependence indicates an increase in the dc conductivity of the samples with increasing temperature.

As shown in Fig. 3(b), similar to Z', Z'' also decreases with increasing frequency or temperature. At 100 °C, a weak peak appeared in Z'' at intermediate frequency of around 100 kHz (inset of Fig. 3(b)). This peak became weaker in intensity and shifted to higher frequencies at increased temperature i.e. this peak exhibited the Debye-type behavior, indicating the existence of relaxation process in the system. The frequency of the maximum f_m (relaxation frequency) shifted to higher values with increasing temperatures, indicating the increasing loss in the sample. This also reflected the decreasing relaxation times (τ), which are calculated from the relaxation frequencies i.e. $f_m = 1/2\pi\tau$. Based on the results in Fig. 3, τ were calculated to be 4.08 μs, 1.21 μs and 0.81 μs at 100 °C, 175 °C and 200 °C, respectively.

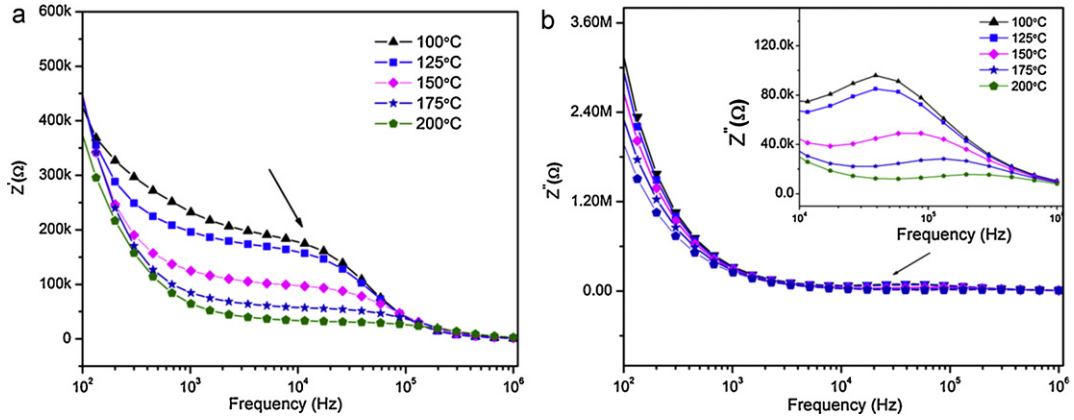

Fig. 3. Temperature and frequency dependent real (a) and imaginary impedance spectra (b) of PZT–NZFO composite ceramic. (Inset: high frequency range of (b) which magnifies the peak positions).

The occurrence of relaxation peaks in the imaginary part of the complex impedance at intermediate frequency range (marked with arrows in Fig. 3) might be due to the existence of the space–charge layer in the sample. Space–charge polarization mechanism is known to predominate in heterogeneous structures, where a material is assumed to be composed of different structures or regions (grain and grain boundaries) [22]. In the present work, XRD analysis showed that the sample consists of two phases, namely, the ferroelectric PZT and the ferrite NZFO. The two phases have different electrical conductivity and thus accumulation of charges will be occurred at the phase boundary. These point charges result in an additional space charge polarization i.e. Maxwell–Wagner (MW-type) relaxation in the frequency range (10 Hz to 1 MHz) [23,24]. Therefore, it is reasonable to assume that the peak is originated from the Maxwell–Wagner polarization between the PZT phase with higher resistivity and the NZFO phase with much lower resistivity. The relaxation frequency obeys the Arrhenius relation and is given by [25],

$$\omega_{\max} = \omega_0 \exp\left(\frac{-E_\tau}{k_B T}\right)$$

$$\omega_{\max} = 2\pi f_m \tag{1}$$

where ω_0 is the pre-exponential factor, E_τ is the activation energy and is calculated to be 0.2821 eV. The relatively low E_τ value obtained in the sample is caused by the space–charge layer existed in this system [26].

Using impedance spectroscopy, one can easily separate the contributions from grain or grain-boundary because each of them has different relaxation times resulting in dissimilar semi-circles in the complex impedance plane. Fig. 4 shows the impedance data taken at different temperatures as a Nyquist diagram (the direction of increasing frequency is indicated). Inset shows the Nyquist diagram magnified at high frequency range and different temperatures. As shown in Fig. 4, two well-defined semicircular arcs were observed at all temperatures except for the curve obtained at 25 °C. At 25 °C, two poorly resolved semicircular arcs were discerned i.e. a small arc at high frequency was largely obscured by a large semicircular arc at low frequency. This might be due to the insulating behavior of the PZT–NZFO ceramic composites. Hence, the following discussion will focus on the temperature range between 100 and 200 °C. As the size of the semicircle in Z^* plot scales according to the magnitude of the resistance, responses possessing large difference in R (often by orders of magnitude) is difficult to be resolved i.e. the more resistive response dominates the Z^* plot entirely making resolution of the less resistive response difficult. Furthermore, as shown in the inset of Fig. 4, it is noticed that as temperature increased the tangent of the smaller semicircle decreased, indicating an increase in the conductivity of the sample. Also, the peak of the semicircle decreased in intensity with increasing temperature, while the frequency for the maximum shifts to higher values with an increase in temperature. Usually, to determine the inter-particle interaction like grain-grain and grain-boundary interaction, the complex impedance can be described using the Cole–Cole formation [27] which is commonly used for polycrystalline materials,

$$Z^* = Z' + iZ'' = \frac{R}{1 + (i\omega/\omega_0)^{1-\alpha}} \tag{2}$$

where α ($0 < \alpha \leq 1$) is the parameter used to calculate the deviation from the ideal Debye-type relaxation. This equation gives rise to the classical Debye's formalism when α goes to zero. Although the composite consists of PZT and NZFO phases, it is not possible to identify each individual phase by its own arc in the impedance or modulus spectrum owing to the proximity of the time constants [28].

Fig. 5 depicts the fitting plot of one representative experimental data at 175 °C. Two semicircle arcs are formed showing the Debye relaxation, suggesting the presence of two relaxation regimes which are attributed to bulk response at high frequencies and grain-boundary response at low frequencies. The grain-boundary response is found to be more effective at low frequencies, while grain response is more effective at high frequencies [28].

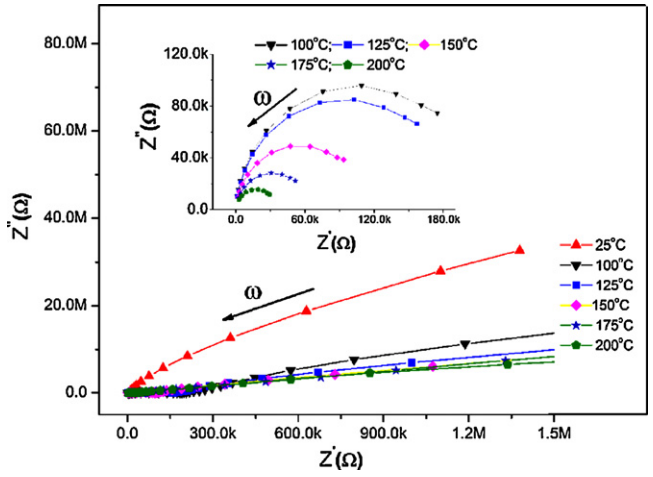

Fig. 4. Nyquist diagram of PZT–NZFO composite at different temperatures. (Inset: Nyquist diagram for PZT–NZFO composite is magnified at high frequency at 100–200 °C).

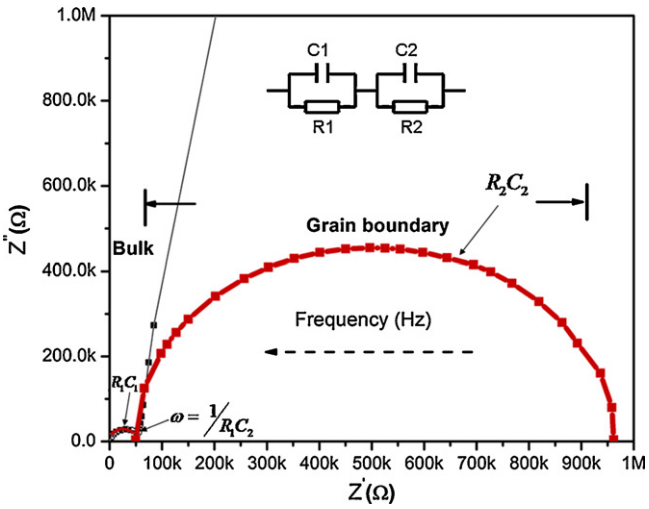

Fig. 5. Cole–Cole fitting plot at temperature of 175 °C for PZT–NZFO composite. (Inset: schematic equivalent electric circuit corresponds to the impedance spectra).

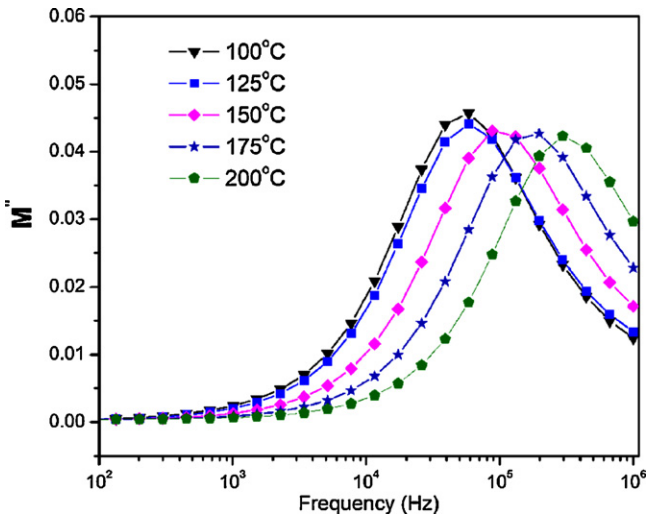

Fig. 6. Temperature dependent imaginary electric modulus spectral of PZT–NZFO composite at various temperatures.

Therefore, the small semicircle at high frequency in the Cole–Cole plot attributed to the grain effect and the large semicircle at low frequency is attributed to the grain-boundary. This behavior can be described by two sub-circuits connected in series as shown in the inset of Fig. 5. Here, the low and high frequency arcs correspond to the R_2C_2 and R_1C_1 responses, respectively. According to the equivalent circuit, the overall impedance can be expressed as

$$Z^* = R_b + \frac{1}{jwC_b} + R_{gb} + \frac{1}{j\omega C_{gb}} \tag{3}$$

$$Z' = \frac{R_b}{(1+\omega_b C_b R_b)^2} \frac{R_{gb}}{(1+\omega_{gb} C_{gb} R_{gb})^2} \tag{4}$$

$$Z'' = \frac{-R_b \omega_b C_b}{1+(\omega_b C_b R_b)^2} + \frac{-R^2 \omega_{gb} C_{gb}}{1+(\omega_{gb} C_{gb} R_{gb})^2} \tag{5}$$

where R_b, R_{gb}, C_b and C_{gb} represent the resistances and capacitances of the bulk (i.e. grain) and grain boundary, respectively, and ω is the angular frequency. The values of R_b (i.e. R_1) and R_{gb} (i.e. R_2) were obtained from the diameter of the semicircle approximately as 50 kΩ and 900 kΩ, respectively. Obviously, our results indicate that the total resistance in the composite is dominated by the grain-boundary resistance (R_{gb}), which is attributed to the fact that the glass phase coated the nano-sized PZT powders and acted as fillers in the composite. This coating might segregate at the interfacial region to provide a relatively high-resistance layer, and is called the grain boundary blocking effect [26]. The capacitances due to these effects can be calculated using the relation

$$\omega\tau = \omega RC = 1 \tag{6}$$

where ω is the angular frequency at the maxima of the semicircle for the components. From the Cole–Cole plot at 175 °C, the values of C_b ($= C_1$) and C_{gb} ($= C_2$, obtained by measuring the value of ω indicated in Fig. 5) were calculated to be about 24 pF and 122 pF, respectively. The relaxation time τ_b (grain) and τ_{gb} (grain-boundary), calculated from Eq. (6), were 1.2 μs and 0.109 ms, respectively. The τ_b calculated from the fitting plot was consistent with the estimated value obtained from the impedance spectra (Z'').

Two semicircles were obtained for the composite sample presented here; each semicircle was corresponded to a resistor–capacitor (R–C) phase. The representation of sample through an electrical analog circuit, such as shown in the inset of Fig. 5 and analytically explained by Eqs. (3–5), is very helpful in representing the electrical features of the sample. Also the capacitance will be generally associated with space charge polarization regions.

3.3. Modulus formalism

The modulus representation is also important in analyzing the electric properties of polycrystalline materials. One advantage of using the electric modulus (M^*) to interpret electric properties is that variation in large values of permittivity and conductivity at low frequencies is minimized. Electric modulus M^* is defined as

$$M^* = \frac{1}{\varepsilon^*} = \frac{1}{\varepsilon' - j\varepsilon''} = \frac{\varepsilon'}{\varepsilon'^2 + \varepsilon''^2} + j\frac{\varepsilon''}{\varepsilon'^2 + \varepsilon''^2} = M' + jM'' \tag{7}$$

and

$$E = M^* D \tag{8}$$

where D is the dielectric displacement (variable) which can be related to the movement of space charge density ρ in a dielectric through:

$$divD = \rho \tag{9}$$

If E preferred, one shall use Eq. (8) in which the electric modulus (M) is the independent variable. The present composite composed of well-conducting grains and poorly conducting grain boundaries and thus favored the accumulation of charges at the boundaries, which consequently increased the polarization by a large interfacial contribution. This resulted in high values of dielectric constant and explained the decrement of dielectric constant with increasing frequency, where the charges at the boundaries cannot reverse orientation as faster as the field.

Fig. 6 shows the imaginary parts of electric modulus (M'') as a function of frequency at various temperatures. M'' possessed a low value at low frequencies (<1 kHz) for all temperatures. This is probably due to the large value of capacitance at low frequencies. On the other hand, at higher frequencies, well-defined peaks were clearly observed and the peak position shifted toward higher frequencies with increasing temperature. The peaks were almost symmetrical exhibiting the behavior of an ideal Debye curve. The relaxation frequencies were found to be 58 kHz and 0.3 MHz at 100 and 200 °C, respectively. Using Arrhenius law, the activation energy E_τ was calculated to be 0.282 eV, which is well agreed with the calculated value based on the imaginary part of impedance (Z'').

The modulus plots of M'' versus M' at different temperatures are shown in Fig. 7(a) and (b). Fig. 7 shows a typical low frequency

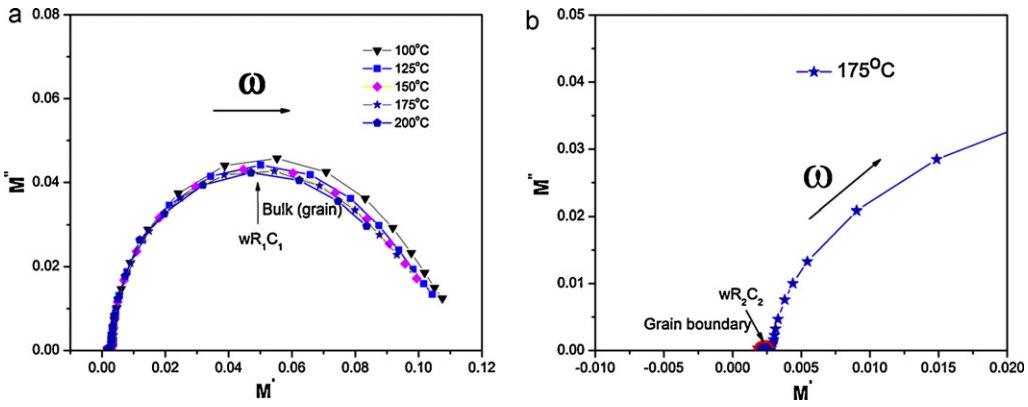

Fig. 7. Temperature and frequency dependent $M'' - M'$ of PZT–NZFO composite (a); the typical one at 175 °C (b).

region modulus plot magnifying the grain boundary contribution at 175 °C. The large semicircle was believed to be induced by the grain effect (R_1C_1), due to the smaller capacitance value dominated in the electric modulus spectra, while the small semicircle might be attributed to the grain boundary effect (R_2C_2). For clarity, the value of C_1 can be extracted from the semicircular arc intercepts on the M' axis in Fig. 7(a), the values of C_1 and f_{max} were used to calculate R_1 using Eq. (6). For the typical temperature at 175 °C, the calculated C_1 and R_1 were about 16 pF and 50 kΩ, which were almost agreed with the values calculated by the Cole–Cole plot in Fig. 5. From the calculated capacitance C_1, we conclude that the large resolved semicircle arc attributed to the bulk response at high frequency.

General speaking, semicircle with a symmetric profile indicates that relaxation exists in the system. Based on the model of Brankovic et al. [29], if an interfacial polarization phenomenon is dominated in the system, the existence of an inhomogeneous distribution of charge carriers in the vicinity of the grain boundary will be resulted. A distorted grain boundary arc (similar to the curve in Fig. 7(b)) will be observed. Therefore, it is concluded that the distortion in the grain boundary arc in this case originates from the distribution of impedance over the space–charge layers adjacent to a charged grain boundary.

3.4. Dielectric analysis

In order to further investigate the relaxation phenomena in this composite, the dielectric constant and loss tangent as a function of frequency at different temperatures are presented in Fig. 8. The dielectric constant was increased with temperature but decreased with escalated frequency. For example, at 1 MHz, the dielectric constant increased from 9 to 11 when the temperature was raised from 100 to 200 °C; while at 100 Hz, the dielectric constant increased from 341 to 600 under the same temperature range. This indicates a low frequency dispersion phenomenon observed in the dielectric constant profiles. The observed dispersion of the dielectric constant might be caused by the hopping of charge carriers among localized states [30], indicating an increase in the ac conductivity along with frequency. In addition, a dielectric relaxation behavior was also observed at the frequency range of 1 kHz to 1 MHz. This was reflected in the loss tangent (tan δ, δ is the phase angle) curves, where well-defined and symmetrical peaks were observed. These peaks shifted to higher frequencies with an increase in temperature and exhibited distributions of Debye-like relaxation processes, which is consistent with the Maxwell–Wagner relaxation dispersion model [22–24]. A decrease in ε' with increasing frequency was also noticed and this might be due to the dipole (space–charge) lags behind the applied field at high frequencies.

The frequency variation of the imaginary part of the dielectric constant (ε'') was calculated using the relation [31].

$$\varepsilon'' = \varepsilon' \tan \delta \tag{10}$$

Fig. 9(a) shows the plots of the real part (ε') versus the imaginary part (ε'') of the complex permittivity i.e. Cole–Cole plot, and Fig. 9(b) shows the high frequency magnified Cole–Cole plot at 175 °C along with the fitting curve. For the quantitative analysis of the dielectric spectra, the Cole–Cole equation was used [27]:

$$\varepsilon^* = \varepsilon_\infty + \frac{\varepsilon_s - \varepsilon_\infty}{1 + (i\omega\tau)^{1-h}} \tag{11}$$

where ε_∞ is the high frequency limit of the dielectric constant, $\varepsilon_s - \varepsilon_\infty$ is the dielectric strength, τ is the mean relaxation time and h represents the distribution of relaxation time ($0 \le h \le 1$). The parameter h is determined from the angle subtended by the radius of the Cole–Cole circle with the ε' axis passing through the origin of the ε''-axis. The Cole–Cole plots in Fig. 9 show three features. Firstly, h is found to be close to 0.5, indicating the polydispersive nature of the dielectric relaxation in the system. This is coincide with the conclusion drawn from the Cole–Cole plot of $Z'' - Z'$. Secondly, the apparent Debye-like relaxation (i.e. MW-type relaxation) existed. Thirdly, a symmetrical broadening of the line-width ($\varepsilon_s - \varepsilon_\infty$) was observed with increasing temperature, indicating the conductivity increases with increasing temperature. A similar trend was also observed in the impedance spectra (Fig. 4). At and above 150 °C, the spectral intensity of the dielectric relaxation (another faint

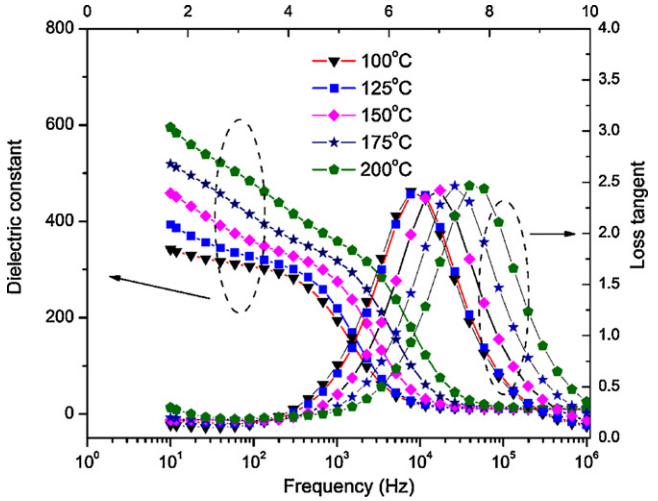

Fig. 8. Temperature and frequency dependent dielectric constant and loss tangent of PZT–NZFO composite.

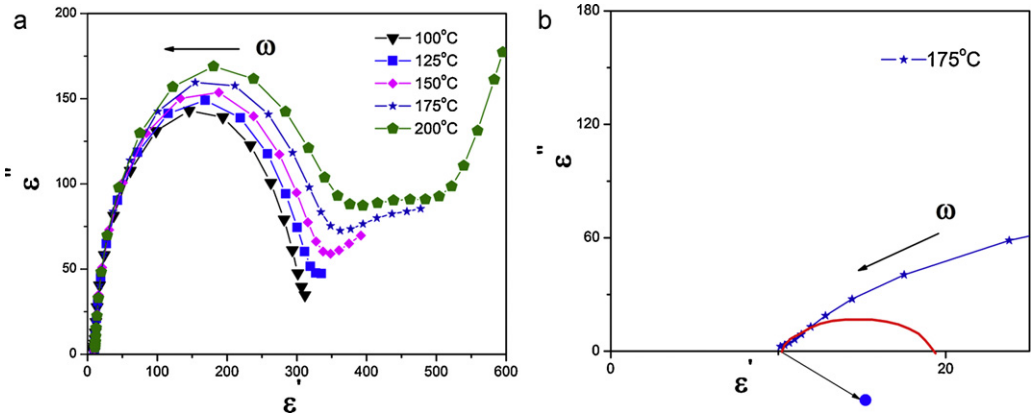

Fig. 9. Cole–Cole plots at various temperature for PZT–NZFO composite (a); the typical one Cole–Cole plot at the temperature of 175 °C is magnified at high frequency, along with the fitting curve of the experimental data (b).

relaxation behavior) at low frequency (<1 kHz) was activated thermally. This suggests the hopping process of charge carriers and small polarons in the multigrain ceramics. In addition, when the temperature reached to 200 °C, the Cole–Cole plot shows the behavior of electrical conductivity at the frequency below 100 Hz (i.e. dc conductivity) which can be attributed to ionic conduction based on the jump relaxation model [32].

3.5. ac conductivity analysis

Fig. 10 shows the ac conductivity plots as a function of frequency at different temperatures. The ac conductivity of the sample was calculated using the standard relation:

$$\sigma_{ac} = \omega\varepsilon'\varepsilon_0 \tan\delta \quad (12)$$

where ε_0 and ε' are the permittivity of the free space and real part of measured dielectric permittivity, respectively. As shown in Fig. 10, the conductivity increased with frequency and became saturated at high frequency. The conductivity values increased from 2.26×10^{-10} and $9.69 \times 10^{-10}\ \Omega^{-1}\ cm^{-1}$ to 5.74×10^{-7} and $2.09 \times 10^{-6}\ \Omega^{-1}\ cm^{-1}$ at 100 °C and 200 °C, respectively, with frequency increased from 10 Hz to 1 MHz. These increments belong to normal thermal mechanism. Low conductivity observed in this system might be attributed to two reasons: one is dense and homogeneous finer structure obtained at low sintering temperature; the other is the glass phase additives in the composite lead to an additional contribution to the scattering from the small amount of glass phase formed at grain boundaries, resulting in poor conductivity [26]. As shown in Fig. 10, there was a strong rise at low frequencies (below 1 kHz), which is due to the grain boundary blocking effect [21]. At 200 °C, low frequency conductivity curve tended to slightly flatten suggesting the dc conductivity behavior (in here, the temperature is not high enough (above 200 °C) to exhibit the more evidences of this frequency independent conductivity due to the limitation of the equipment). This is consistent with the low frequency slop in the Cole–Cole plot (Fig. 9). The conductivity curves at the intermediate frequency (5 kHz) were merging together and showed a linearly increase at all temperatures (marked with arrow). Lastly, for high frequencies (>10 kHz), the conductivity became saturated; the completing relaxation processes visualized a temperature dependent dispersion behavior. This is corresponding to the dielectric relaxation in Figs. 8 and 9, which is ascribed to the bulk conductivity relaxation. The conductivity depends on frequency according to the 'universal dynamic response' for ionic conductors [33] given by the phenomenological law:

$$\sigma(\omega) = \sigma_{dc} + A\omega^n \quad (13)$$

where σ_{dc} is the dc bulk conductivity, A is a thermally activated quantity, and n the frequency exponent and can be taken a value <1. It is typical of thermal assisted tunneling between localized states. As shown in Fig. 10, the conductivity was observed to increase with frequency, linear variation of ac conductivity indicated that the conduction occurs by hopping of charge carriers and small polaron among localized states. The dispersion in conductivity at high frequency may be due to the MW-type polarization, caused by interfacial polarization due to spatial variants of the conductivity of the material.

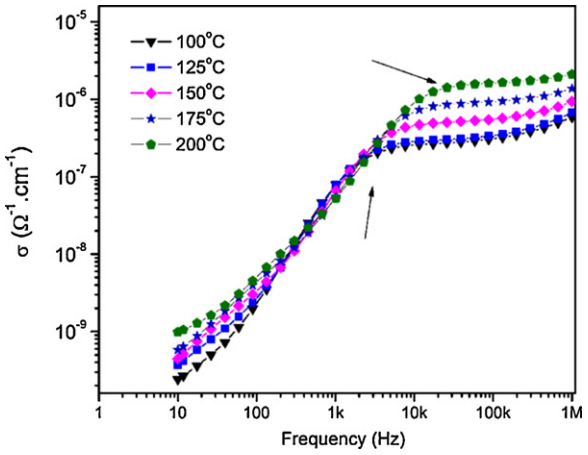

Fig. 10. Temperature dependent ac conductivity spectra (σ') of PZT–NZFO composite at 100–200 °C.

4. Conclusions

High-quality fine-grained magnetoelectric $Pb(Zr_{0.53}Ti_{0.47})O_3$–$(Ni_{0.5}Zn_{0.5})Fe_2O_4$ (PZT–NZFO) composites have been successfully fabricated by a modified hybrid process. The coexistence of PZT and NZFO phases was identified by XRD. Impedance spectroscopy and electric modulus analysis indicate the contributions from grain and grain boundary effect at different frequencies. Activation energy calculated from the two methods was in good agreement with each other. Also, the Debye-like relaxation was also observed in the impedance loss spectra. The total bulk resistivity was dominated by the grain boundary due to the glass phase additive in the matrix. This was also reflected by a small value of conductivity obtained in ME composite, suggesting the effect of glass additive on the modification of the grain boundary properties. Dielectric spectra revealed

a poly-dispersive nature of dielectric relaxation existing in the system. The polaron relaxation at low frequency <1 kHz and MW-type dispersion at intermediate frequency range were discussed. Furthermore, the conductivity spectra revealed different contributions to the conductivity; the low frequency conductivity was due to the hopping of charge carriers and small polaron, the intermediate frequency conductivity was due to the MW-type polarization caused by spatial variants of the conductivity of the material i.e. the space–charge effect.

Acknowledgement

This research was partially supported by the Hong Kong Polytechnic University (Grant GU-694).

References

[1] G. Srinivasan, E.T. Rasmussen, J. Galleges, R. Sirnivasan, Phys. Rev. B 64 (2001) 214408.
[2] M. Figebig, J. Phys. D 38 (2005) 123.
[3] W. Eerenstein, N.D. Mathur, J.F. Scott, Nature (London) 442 (2006) 759–765.
[4] M. Atif, M. Nadeem, R. Grössinger, R.S. Turtelli, J. Alloys Compd. 509 (2011) 5720–5724.
[5] V.J. Folen, G.T. Rado, E.W. Stalder, Phys. Rev. Lett. 6 (1961) 607–608.
[6] H.L. Zhang, X.M. Chen, T. Wang, F.F. Wang, W.Z. Shi, J. Alloys Compd. 500 (2010) 46–48.
[7] J.V. Suchetelene, Philips Res. Rep. 27 (1972) 28–37.
[8] D.V. Chashin, Y.K. Fetisov, K.E. Kamentsev, G. Srinivasan, Appl. Phys. Lett. 92 (2008) 102511.
[9] Y.J. Wang, F.F. Wang, S.W. Or, W.H.L. Chan, X.Y. Zhao, H.S. Luo, Appl. Phys. Lett. 93 (2008) 113503.
[10] H.F. Zhang, S.W. Or, W.H.L. Chan, J. Appl. Phys. 104 (2008) 104109.
[11] H.F. Zhang, S.W. Or, W.H.L. Chan, Y. Fang, J. Eur. Ceram. Soc. 31 (2011) 1753–1761.
[12] H.F. Zhang, S.W. Or, W.H.L. Chan, J. Alloys Compd. 509 (2011) 6311–6316.
[13] L.M. Hrib, O.F. Caltun, J. Alloys Compd. 509 (2011) 6644–6648.
[14] W.C. Liu, C.L. Mak, K.H. Wong, C.Y. Lo, S.W. Or, W. Zhou, A. Hauser, F.Y. Yang, R. Sooryakumar, J. Phys. D: Appl. Phys. 41 (2008) 125402.
[15] V.M. Petrov, M.I. Bichurin, in: F. Manfred, V.E. Victor, E.C. Irina (Eds.), Magnetoelectric Interaction Phenomena in Crystals, Proceedings of the NATO ARW on Magnetoelectric Interaction Phenomena in Crystals, Sudak, Ukraine, September 21–24, 2003, 2004, pp. 65–70.
[16] H.G. Pan, Y.F. Liu, M.X. Gao, Y.Q. Lei, Q.D. Wang, J. Electrochem. Soc. (2005) A326–A332.
[17] Y.F. Liu, H.G. Pan, M.X. Gao, R. Li, X.Z. Sun, Y.Q. Lei, J. Alloys Compd. 508 (2005) 109–119.
[18] O. Raymond, R. Font, N. Suarez-Almodovar, J. Portelles, J.M. Siqueiros, J. Appl. Phys. 97 (2005) 084108.
[19] K. Srinivas, P. Sarah, S.V. Suryanarayana, Bull. Mater. Sci. 26 (2003) 274.
[20] N. Ortega, A. Kumar, P. Bhattacharya, S.B. Majumder, R.S. Katiyar, Phys. Rev. B 77 (2008) 014111.
[21] W. Chen, W. Zhu, C. Ke, Z. Yang, L. Wang, X.F. Chena, O.K. Tan, J. Alloys Compd. 508 (2010) 141–146.
[22] O. Bidault, P. Goux, M. Kchikech, M. Belkaoumi, M. Maglione, Phys. Rev. B 49 (1994) 7868.
[23] N. Ortega, A. Kumar, R.S. Katiyar, J.F. Scott, Appl. Phys. Lett. 91 (2007) 102902.
[24] J.X. Zhang, J.Y. Dai, H.L.W. Chan, J. Appl. Phys. 107 (2010) 104105.
[25] L. Zhang, Z.J. Tang, Phys. Rev. B 70 (2004) 174306.
[26] X. Guo, W. Sigle, J. Fleig, Solid State Ionics 154–155 (2002) 555–561.
[27] K.S. Cole, R.H. Cole, J. Chem. Phys. 9 (1941) 341.
[28] J.R. Macdnoald, Impedance Spectroscopy: Emphasizing Sold Materials and Systems, John Wiley & Sons Inc., 1987.
[29] G. Brankovic, Z. Brankovic, V.D. Jovic, J.A. Varela, J. Electroceram. 7 (2001) 89.
[30] D. Adler, J. Feinleib, Phys. Rev. B 2 (1970) 3112.
[31] V. Hipple, Dielectrics and Waves, New York, Wiley, 1954.
[32] A.K. Jonscher, Nature (London) 267 (1997) 673.
[33] J. Grigas, Microwave Dielectric Spectroscopy of Ferroelectrics and Related Materials, Gordon and Breach Publn. Inc., Amsterdam, 1996.